ACS OMEGA

http://pubs.acs.org/journal/acsodf

Article

Interaction of Prion Peptides with DNA Structures

Anshula Tandon,[‖] Vinod Kumar Subramani,[‖] Kyeong Kyu Kim,* and Sung Ha Park*

Cite This: *ACS Omega* 2022, 7, 176−186

Read Online

ACCESS | Metrics & More | Article Recommendations

ABSTRACT: Prion protein aggregation is known to be modulated by macromolecules including nucleic acids. To clarify the role of nucleic acids in PrP pathology, we investigated the interaction between nucleic acids and the prion peptide (PrP)—a synthetic prion protein model peptide resembling a portion of the human prion protein in structure and function spanning amino acid residues 106−126. We used synthetic DNA lattices and natural DNA duplexes extracted from salmon (sDNA) bound with PrP and studied their interaction using distinct physical measurements. The formation of DNA lattices with PrP was visualized by atomic force microscopy (AFM) to investigate the influence of the PrP. PrP inhibited the growth of the double-crossover (DX) lattices significantly compared to the control peptide (CoP). We also conducted optical measurements such as ultraviolet−visible (UV−Vis), circular dichroism (CD), and Fourier transform infrared (FTIR) spectroscopies to validate the interaction between PrP and DNA immediately (D_0) and after a 30-day incubation (D_{30}) period. UV−Vis spectra showed variation in the absorbance intensities, specific for the binding of CoP and PrP to DNA. The CD analysis revealed the presence of various secondary structures, such as α-helices and β-sheets, in PrP- and PrP-bound sDNA complexes. The PrP−sDNA interaction was confirmed using FTIR by the change and shift of the absorption peak intensity and the alteration of PrP secondary structures in the presence of DNA. The cytotoxic effects of the PrP-bound sDNA complexes were assessed by a cytotoxicity assay in human neuroblastoma cells in culture. It confirmed that PrP with sDNA was less cytotoxic than CoP. This study provides new applications for DNA molecules by investigating their effect in complex with aggregated proteins. Our study unequivocally showed the beneficial effect of the interaction between DNA and the pathological prion protein. It therefore provides valuable information to exploit this effect in the development of potential therapeutics. Moreover, our work might serve as a basis for further studies investigating the role of DNA interactions with other amyloidogenic proteins.

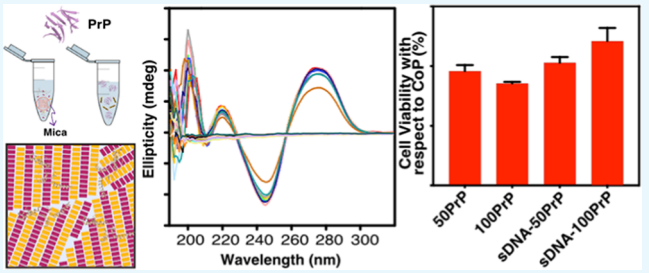

INTRODUCTION

Prion diseases are fatal transmissible spongiform encephalopathies affecting humans and animals. They can be of infectious, genetic, or sporadic nature and are characterized by protein aggregation and neurodegeneration.[1] They result from the conformational conversion of the normal cellular isoform of the prion protein, which displays a high α-helix content, to an insoluble scrapie isoform rich in β-sheet content.[2] The cellular isoform of the prion protein displays less aggregation propensity than the scrapie form.[3−5] The process of prion protein aggregation is modulated by a set of macromolecules[6−10] including nucleic acids.[11,12] DNA is known for its catalytic role in aggregation and propagation of prion proteins and is considered as one of the promising prion protein molecular partners.[13] Besides, cellular isoforms of prion play an important physiological role in protecting cells against reactive-oxygen-species-mediated DNA damage and perform DNA damage repair in neuronal cells by stimulating AP endonuclease 1 DNA repair activity.[14,15] *In vitro*, DNA binds to both cellular and scrapie prion proteins; however, this interaction is nonspecific as the prion protein interacts with a wide repertoire of nucleic acids with varied sequences and structures.[8,16−18] Interestingly, DNA binding to a prion protein leads to conformational changes of the protein from the α to β isoform.[8,19,20] The prion protein-bound DNA complex is toxic to cells in culture, is proteinase K-resistant and undergoes amyloid oligomerization.[18,21] However, some synthetically modified oligonucleotides seem to reverse prion infectivity in cell-based assays and prion animal models.[22,23] Therefore, the actual role of DNA molecules in prion pathophysiology remains unclear.

As crystallographic or pathophysiological data for prion protein-bound DNA complexes are lacking, the synthesis of DNA lattices containing the periodicity of the building blocks might be useful to directly visualize DNA structures in the

Received: August 11, 2021
Accepted: November 9, 2021
Published: December 20, 2021

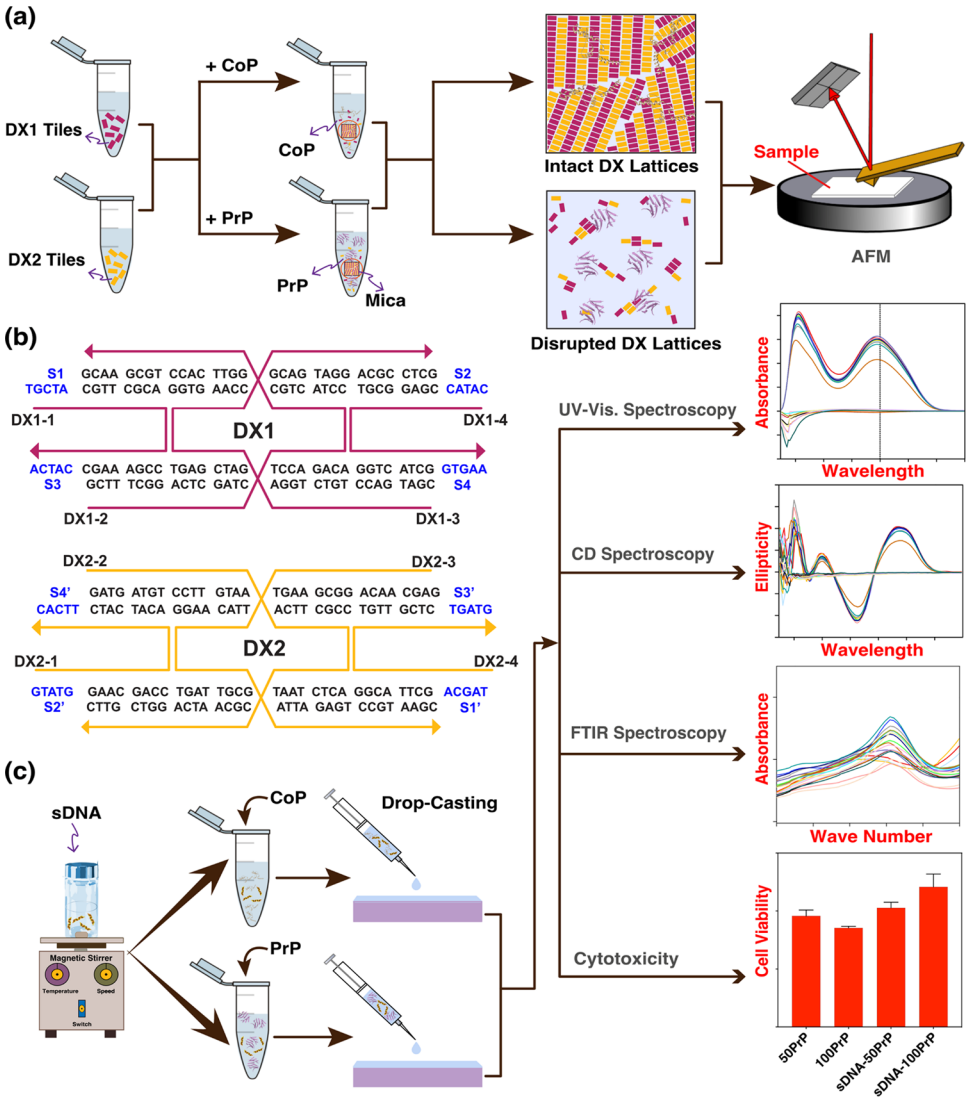

Figure 1. Schematic representations of the procedures involved during sample preparation of CoP- and PrP-bound DNA complexes and representative data of the physical measurements. (a) Preparation of CoP- and PrP-bound double-crossover lattices (DX-CoP and DX-PrP, respectively) formed by a mica-assisted growth method. AFM was used to test the topological variance of DX-CoP and DX-PrP lattices. (b) Schematic illustration of DX tiles (DX1 and DX2 containing 4 DNA strands each) base sequences used for the formation of DNA DX lattices. The complementary set (S# and S#′) of sticky-end sequences is indicated in blue. (c) Construction of CoP- and PrP-bound sDNA thin films and representative data of the physical measurements. CoP- and PrP-bound sDNA thin films were formed using the drop-casting method. Physical characteristics of the samples were measured by ultraviolet−visible (UV−Vis), circular dichroism (CD), and Fourier transform infrared (FTIR) spectroscopies.

presence of the cellular or scrapie form of the prion protein. In addition, naturally available DNA duplexes such as DNA extracted from salmon (sDNA) which are low-cost and biodegradable, are also beneficial.[24,25] The prion protein region spanning residues 106−126 in humans display specific characteristics. This region has been identified as highly amyloidogenic and induces neurotoxicity in primary cultures of rat hippocampal neurons, cortical neurons, cerebellar cells, and cultured human neuroblastoma cells.[26−28] It also has the capacity to readily form fibrils,[26] being partially resistant to proteolysis[4] compared to a control peptide (CoP) generated as a randomized version with the same composition as PrP.[28] Based on these observations, this prion peptide (PrP) has been used as a model to study the mechanisms of prion disease propagation and transmission.[3,4,26,29−31] Interestingly, it has been shown that PrP interaction with DNA induced its polymerization and aggregation.[19,32]

Here, we used PrP bound to synthetic DNA lattices (formed of rectangle-shaped double-crossover (DX) DNA building blocks) and natural DNA duplexes extracted from salmon (sDNA). Atomic force microscopy (AFM) was used to investigate the topological characteristics of DX lattices bound with various concentrations of CoP ([CoP]) and PrP ([PrP]). To validate the interaction between PrP and DNA immediately after mixing them (D_0) and after a 30-day incubation (D_{30}) period, physical measurements such as ultraviolet−visible (UV−Vis), circular dichroism (CD), and Fourier transform infrared (FTIR) spectroscopies were conducted. Finally, a cytotoxicity assay was performed on human neuroblastoma cells in culture to verify the effect of the PrP−sDNA complexes on cell physiology.

https://doi.org/10.1021/acsomega.1c04328
ACS Omega 2022, 7, 176−186

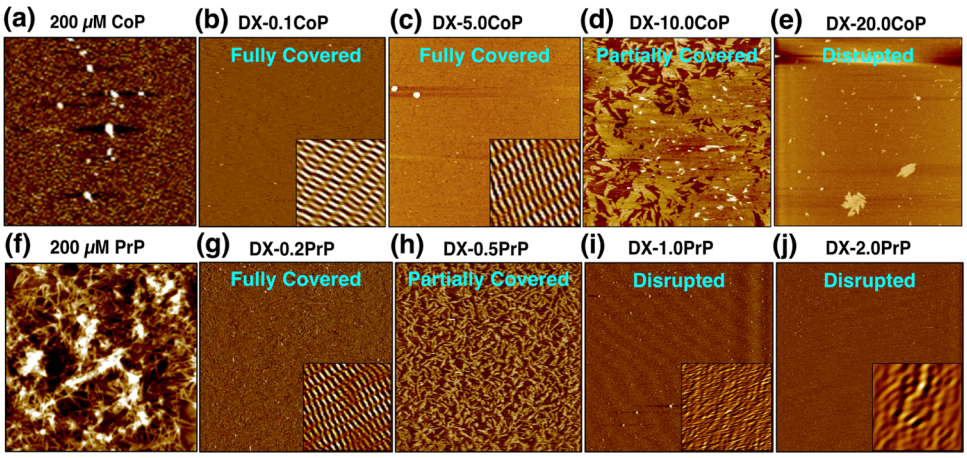

Figure 2. Topological characteristics of DX lattices grown on mica with various [CoP] and [PrP]. (a) Representative AFM image of the pristine CoP at 200 μM. (b, c) Fully covered DX lattices with 0.1 and 5.0 μM CoP are labeled DX-0.1CoP and DX-5.0CoP, respectively. (d) Partially covered DX lattices with 10.0 μM CoP. (e) Disrupted DX lattices in the presence of a relatively higher [CoP] (20.0 μM). (f) AFM image of the pristine PrP (200 μM). (g) Fully covered DX lattices with 0.2 μM PrP (DX-0.2PrP). (h) Partially covered DX lattices with 0.5 μM PrP (DX-0.5PrP). (i, j) Disrupted DX lattices with 1.0 and 2.0 μM PrP (DX-1.0PrP and DX-2.0PrP, respectively). Scan sizes of all AFM images are 5 μm × 5 μm. Inset images (scan size of 100 nm × 100 nm) constructed by noise-filtered reconstructed fast Fourier transform (FFT) display material of crystalline (shown in (b), (c), and (g)) and amorphous (i, j) nature.

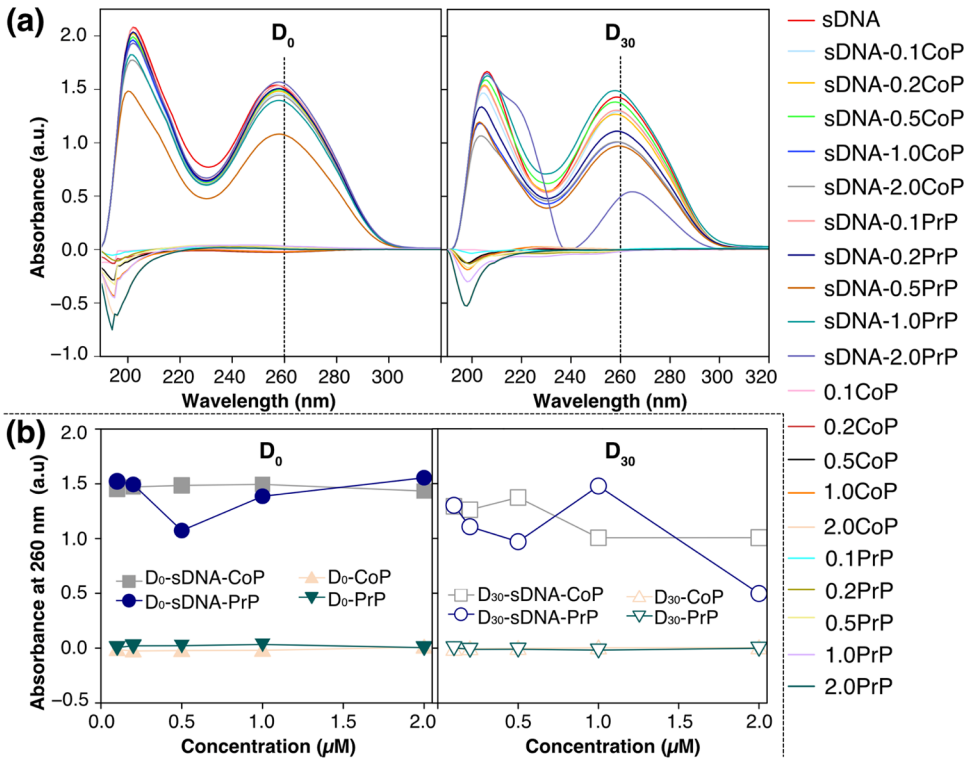

Figure 3. UV−Vis absorbance of CoP- and PrP-bound sDNA duplexes in solution without (D_0) and with 30-day incubation (D_{30}). (a) Absorbance of sDNA duplexes bound with various [CoP] and [PrP]. To understand the interaction between PrP and sDNA, samples were incubated between 0 and 30 days at room temperature. (b) Absorbance at 260 nm of sDNA duplexes bound with various [CoP] and [PrP] measured at D_0 and D_{30}.

RESULTS AND DISCUSSION

Preparation and Characterization of CoP- and PrP-Bound DNA Complexes. Figure 1 details the sample preparation of PrP-bound DX lattices by a surface-assisted growth method and of PrP-bound sDNA thin films through drop-casting. Construction of PrP-bound DX lattices on mica was carried out following a two-step annealing method, the first annealing step to construct individual DX tiles in solution and the second step to hybridize PrP-bound DX lattices with mica.[33] To examine the influence of CoP and PrP oligopeptides during the formation of DNA structures, the surface topology of DX lattices bound to CoP and PrP was examined by AFM. In addition, solution samples consisting of sDNA dissolved in deionized water with various [CoP] and [PrP] were prepared.

The structural stability of the sDNA, the secondary structure of PrP, and the interaction between sDNA and PrP were assessed by UV−Vis, CD (measurement of solution samples),

https://doi.org/10.1021/acsomega.1c04328
ACS Omega 2022, 7, 176−186

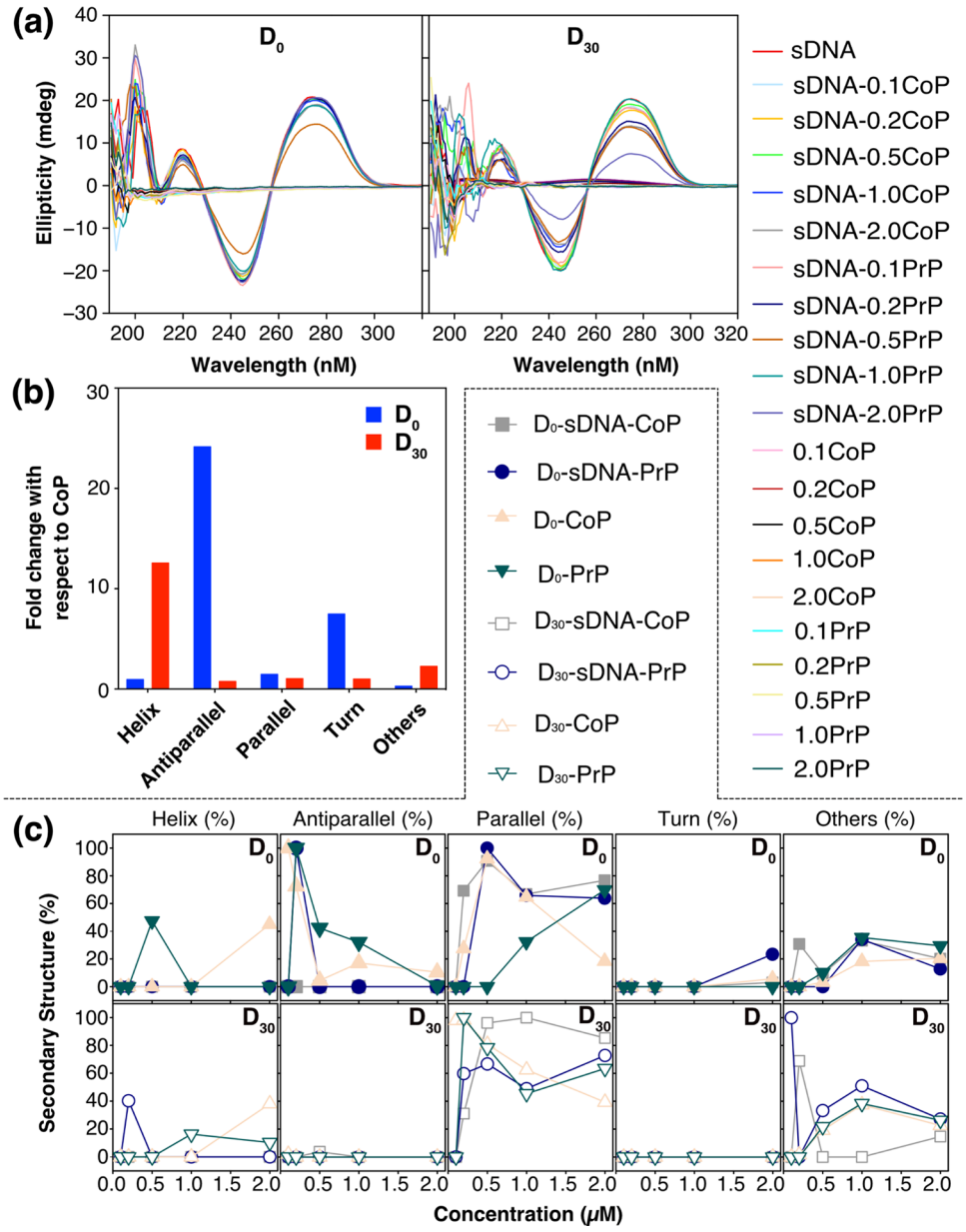

Figure 4. CD spectra and secondary structure components of PrP with sDNA in solution with no incubation (D_0) and after a 30-day incubation (D_{30}) period. (a) Ellipticities of pristine PrP, pristine sDNA, and PrP-bound sDNA solutions as a function of wavelength measured at D_0 and D_{30}. (b) Secondary structure components expressed as the ratio of PrP to CoP at D_0 and D_{30}. The cumulative values of the predicted secondary structures across different concentrations at D_0 and D_{30} were used to determine the ratio. (c) Percentage of the PrP secondary structure components, such as helices, antiparallel β-sheets, parallel β-sheets, and β-turns as a function of PrP concentrations. The PrP secondary structures were quantified by processing the measured CD data using the BeStSel algorithm.

and FTIR spectroscopies (measurement of thin-film samples formed by drop-casting) of CoP- and PrP-bound sDNA duplexes. We also performed the measurements with CoP- and PrP-bound sDNA solutions, which were left to interact for 30 days at room temperature (D_{30}) or not (D_0). Finally, cell cytotoxicity was tested on human neuroblastoma cells treated with pristine PrP peptides and PrP-bound sDNA solutions.

Topological Characteristics of DX Lattices Grown on a Substrate with Various [CoP] and [PrP]. Topological structures of pristine CoP and PrP oligopeptides, as well as DX lattices, were imaged by AFM. We noticed clear topological differences, such as nonaggregating globular structures for CoP, aggregated fibrous structures for PrP, and 2D crystalline structures for DX lattices (Figure 2a,f). Interestingly, PrP formed large aggregates of long, continuous fibrils appearing as dense mesh works as reported previously.[30,34] For polycrystalline DX lattices formed by the surface-assisted growth method, the full coverage of 5 mm × 5 mm DX lattices on mica was reached for a concentration (known as saturation concentration) of 20 nM for each tile.[35]

We tested the self-assembly of DX lattices in the presence of CoP and PrP, which might severely affect the formation of DX lattices due to their specific binding characteristics. Interestingly, fully covered, partially covered, and disrupted DX lattices on mica were observed for different [CoP] and [PrP]. For CoP, fully covered DX lattices were achieved at a concentration of up to 5.0 μM, and disrupted DX lattices were induced by [CoP] above 20 μM (Figure 2b–e). For PrP,

https://doi.org/10.1021/acsomega.1c04328
ACS Omega 2022, 7, 176−186

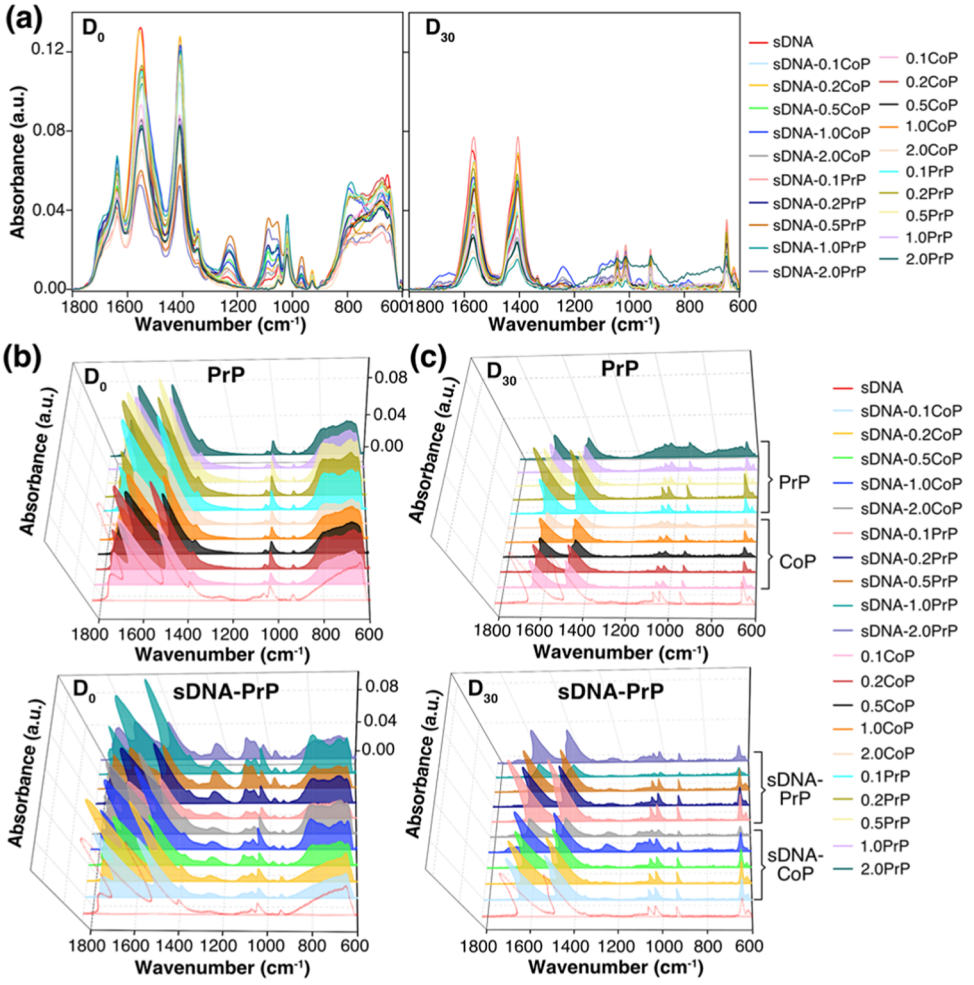

Figure 5. FTIR spectra of the PrP- and PrP-bound sDNA thin films. (a) FTIR spectra of the PrP- and PrP-bound sDNA thin films with no (D_0) and after 30 days of incubation (D_{30}). (b) (top) 3D representations of FTIR spectra of the sDNA and pristine PrP thin films and (bottom) the PrP-bound sDNA thin films formed by drop-casting with no incubation (D_0). (c) (top) 3D representations of FTIR spectra of the sDNA and pristine PrP thin films and (bottom) the PrP-bound sDNA thin films after a 30-day incubation (D_{30}) period.

concentrations up to 1.0 μM were required to obtain fully covered DX lattices and above 1.0 μM for disrupted DX lattices (Figure 2g–j). Crystalline (periodicity shown in Figure 2b,c,g) and amorphous (no periodicity, Figure 2I,j) characteristics of PrP-bound DX lattices are shown in inset images constructed from the data processed by noise-filtering and fast Fourier transform (FFT). We noticed that PrP contributed to the growth inhibition of the DX lattices 20 times more than CoP. The complementary sticky-end hybridization between tiles during the second annealing step might be more severely inhibited by the aggregated fibrous PrP than by CoP. Consequently, an incomplete or compromised growth of the DX lattices on a given substrate might occur.

UV–Vis Absorbance of CoP- and PrP-Bound sDNA Duplexes in Solution without (D_0) and with 30-Day Incubation (D_{30}). To understand the relative strength of the interaction between PrP and sDNA immediately or 30 days after mixing them, we examined the UV–Vis absorbance of CoP- and PrP-bound sDNA duplexes. Figure 3a shows the UV–Vis absorbance of CoP- and PrP-bound sDNA duplexes in solution after buffer subtraction. Two absorption peaks typical for DNA were noticed at 210 and 260 nm. These peaks arise from the n to π^* transition of the DNA phosphate backbone and from the π to π^* transition of the base pairs, respectively (Figure 3a). The interaction of PrP with sDNA induced fluctuations in the UV–Vis absorbance intensities (as compared to the pristine DNA), which reflected the binding characteristics of CoP and PrP to DNA. PrP showed larger fluctuations of the absorbance intensities than CoP, which indicated a stronger interaction of PrP with DNA compared to CoP. This affected the stability of the DNA structure. The fluctuation of absorbance intensities can be significantly increased by incubating PrP with DNA for a longer time. For instance, the absorbance intensity of PrP-bound sDNA duplexes obtained with 2 μM of PrP and measured after 30 days (D_{30}-sDNA-2.0PrP) was 70% less than the one measured immediately after mixing (D_0-sDNA-2.0PrP).

CD Spectra and Secondary Structures of PrP with sDNA in Solution at D_0 and D_{30}. Ellipticities of pristine PrP, pristine sDNA, and PrP-bound sDNA solutions measured at D_0 and D_{30} were studied. We analyzed the CD data in the wavelength range of 230–320 nm to gain information about helicity such as the winding angle and base-pair twist of the sDNA duplex. Measurements of the ellipticity intensities of DNA at 255 and 275 nm revealed that the right-handed helicity of DNA remained unchanged in the presence of PrP. However, the winding angle and base-pair twist of the sDNA duplexes were affected by the PrP isoform (stronger effect of

https://doi.org/10.1021/acsomega.1c04328
ACS Omega 2022, 7, 176–186

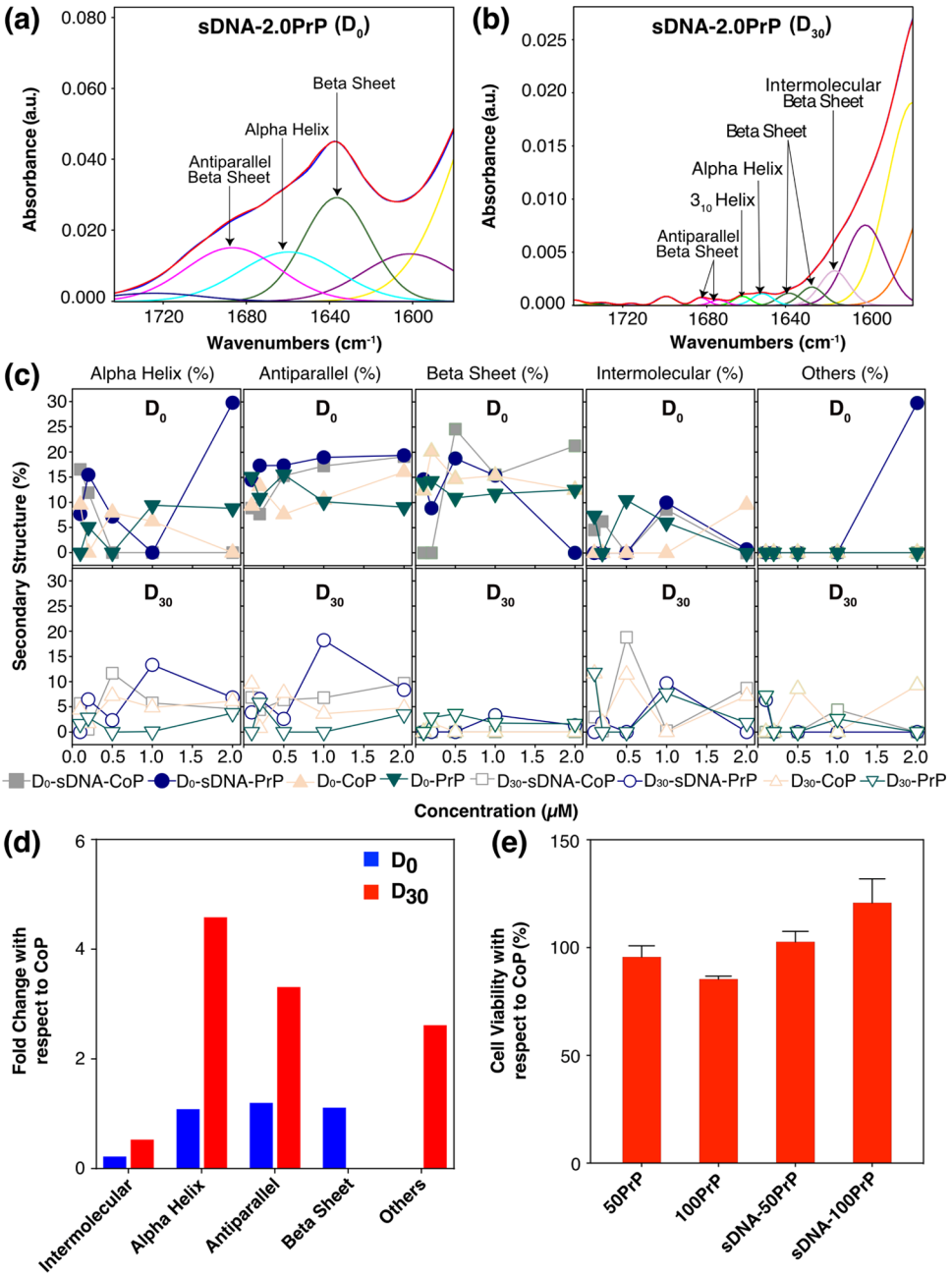

Figure 6. Deconvolution of FTIR spectra, secondary structures of PrP in sDNA thin films at D_0 and D_{30}, and cell viability of CoP- and PrP-bound sDNA duplexes. (a, b) Deconvolution of resolution-enhanced FTIR spectra of the amide I band of sDNA-2.0PrP at D_0 and D_{30}. Deconvolution FTIR spectra showing the emergence of three peaks at D_0 and seven peaks at D_{30} in sDNA-2.0PrP thin films. The Fourier self-deconvoluted (FSD) spectrum (blue line) and the curve-fitted spectrum (red) were closely overlapping. (c) Percentage of PrP secondary structures (with and without sDNA) such as helices, antiparallel β-sheets, and intermolecular/aggregated strands as a function of PrP concentration. The PrP secondary structures were quantified by processing the measured deconvolution FTIR spectra using OMNIC software. (d) Ratio of PrP secondary structures with respect to CoP at D_0 and D_{30}. (e) Fold change in viable SH-SY5Y cells treated with PrP. Here, CoP was used as a control.

PrP than CoP), PrP concentration (higher concentrations had a stronger impact), and incubation time with PrP (more significant effect at D_{30} than D_0) (Figure 4a). The CD feature at 255 nm is influenced by the dihedral angle between the deoxyribose and the nitrogenous base of deoxyguanosine.[36] At 275 nm, the amplitude change in ellipticity is associated with a compact arrangement of sDNA duplexes due to the relatively higher percentage of β-structure components within PrP.[37] Therefore, the gradual amplitude reduction at 255 and 275 nm of the CD bands between D_0-sDNA-0.1CoP and D_{30}-sDNA-2.0PrP reflected an increase in the winding angle and a decrease in the base-pair twist.[38]

In addition, the secondary structures of PrP with sDNA in solution were investigated using peptide CD spectroscopy in the 190−250 nm region using the BeStSel algorithm (Figure 4b,c).[39] Changes in the secondary structural components were observed with increasing PrP concentrations (Figure 4c). The cumulative values of the predicted secondary structures across different PrP concentrations at D_0 and D_{30} were used to determine the ratio of PrP with respect to CoP at D_0 and D_{30} (Figure 4b). The presence of β-sheet structures[40] in a protein

https://doi.org/10.1021/acsomega.1c04328
ACS Omega 2022, 7, 176−186

inherently favors the interaction with DNA by allowing hydrogen bonds between the peptide NH groups and deoxyribose-O-3′. Here, a 12-fold increase in the percentage of α-helices (an intrinsic characteristic of CoP) was measured in the PrP samples incubated for 30 days with sDNA (D_{30}) compared to the values obtained immediately after mixing (D_0). This implied a hindrance of PrP aggregation in the presence of DNA. In contrast, the incubation of PrP samples for 30 days (D_{30}) induced a 22-fold reduction of the population of antiparallel β-sheets (intrinsic characteristic of PrP) compared to PrP samples at D_0. The predominant β-sheet components in PrP, which interacted favorably with sDNA, prevented subsequent oligomerization and aggregation.

FTIR Spectra of Pristine PrP- and PrP-Bound sDNA Thin Films. The vibrational spectra of biological molecules, which provide information about the molecular structure and the interaction between molecules, can be determined by the vibrational force fields. Proteins normally exhibit 9 characteristic vibrational frequencies named amides A, B, and I−VII in the order of decreasing frequency. FTIR was employed to gain insights into the vibrational frequencies. Figure 5a shows FTIR absorption spectra of pristine sDNA, PrP, and PrP-bound sDNA thin films obtained at D_0 and D_{30}. For a better understanding, 3D representations of the FTIR spectra are displayed in Figure 5b,c.

Among the vibrational frequencies of proteins, the amide I and amide II bands are the two major bands in the IR spectrum.[41] Absorption bands between 1700 and 1600 cm^{-1} form the amide I region originating from C═O and C−N stretching modes and N−H bending vibrations. Clues about secondary structures such as α-helices, β-sheets, turns, and nonordered structures were obtained by analyzing the amide I region.[41] For instance, FTIR spectra of pristine PrP- and PrP-bound sDNA thin films at D_0 showed prominent peaks in the protein amide I region corresponding to α-helices (1662−1645 cm^{-1}) and β-sheets (1640−1620 cm^{-1})[42] (Figure 5b). These peaks were suppressed by 30 days of incubation (pristine PrP- and PrP-bound sDNA thin films at D_{30}) (Figure 5c). This is attributed to the perturbation of the C═O stretching vibrations, which implies that a significant change in the peptide conformation occurred in the presence of DNA and upon incubation. A prominent peak at 1550 cm^{-1} attributed to the out-of-phase combination of the NH in-plane bend and the CN stretching vibrations[42] was observed in amide II bands. This peak intensity was decreased in pristine PrP- and PrP-bound sDNA thin films at D_{30} similarly to what was observed for the amide I peaks (Figure 5c).

The peaks for pristine PrP- and PrP-bound sDNA thin films at D_0 found below 1500 cm^{-1} (one conspicuous peak at 1409 cm^{-1} and another at 1343 cm^{-1}) belong to the fingerprint amide III region of the spectrum arising due to N−H in-plane bending and CN stretching vibrations. After a 30-day incubation period, these peak intensities (i.e., pristine PrP- and PrP-bound sDNA thin films at D_{30}) reduce noticeably (Figure 5c). Here, amide III−VII vibrations were measured between 1229 and 200 cm^{-1} and are of little practical use in protein conformational studies.[42]

Pristine sDNA and PrP-bound sDNA thin films showed peak characteristics of DNA molecules at 1224 cm^{-1} (representing the asymmetric phosphate vibration), 1100−1050 cm^{-1} (representing the asymmetric phosphate vibrations in DNA), and 960 cm^{-1} (corresponding to the ribose-phosphate skeletal motion).[43,44] The FTIR intensities of these peaks decreased upon incubation, as observed for PrP-bound sDNA thin films at D_{30}, indicating a probable interaction between DNA and the PrP peptide. The 30-day incubation period provided enough time for the interaction to occur.

Deconvolution of FTIR Spectra and Secondary Structures of PrP in sDNA Thin Films at D_0 and D_{30}. Deconvolution analysis was needed to obtain detailed information for the individual components of the amide I band from the FTIR spectra. FTIR spectroscopy provides the structural features of peptides and proteins, by measuring the wavelength and intensity of the absorption of IR radiation by a sample.[45] However, the resolution of the FTIR spectra is not enough to resolve individual components, such as α-helices and β-sheets, in the amide I band because the number of individual components is usually greater than the separation capacity between the maxima of adjacent peaks. Thus, we adopted a resolution enhancement method based on band narrowing known as Fourier deconvolution (using OMNIC software) for better identification of the overlapping component bands by increasing the separation.[46]

Figure 6a,b shows the FTIR spectra deconvolution of amide I bands for PrP-bound sDNA thin films with 2.0 μM PrP (sDNA-2.0PrP) without (D_0) and with 30-day incubation (D_{30}). We notice that the curve-fitted FTIR spectrum (red) is closely overlapping with the Fourier self-deconvoluted (FSD) spectrum (blue line) as expected. We chose additional 50 cm^{-1} regions on both sides of the amide I (1700−1600 cm^{-1}) as apodization function in the deconvolution procedure to reduce the noise components.[47]

Secondary structures of PrP in sDNA-2.0PrP at D_0, such as β-sheets, α-helices, and antiparallel β-sheets were observed (Figure 6a). β-Sheet (centered at 1636 cm^{-1}) and α-helix (1650 cm^{-1}) components arise due to the formation of intramolecular β-sheets and α-helical proteins, respectively.[42,48−50] Antiparallel β-sheet conformation (centered at 1687 cm^{-1}) was identified toward the high end of the amide I region.[51] For D_{30}, we observed interesting secondary structures of PrP in sDNA-2.0PrP such as intermolecular β-sheets (centered at 1614 cm^{-1}), 3_{10}-helices (1667 cm^{-1}), β-sheets (two peaks at 1625 and 1637 cm^{-1}), α-helices, and antiparallel β-sheets (two peaks at ∼1680 cm^{-1}) (Figure 6b). Intermolecular β-sheets tend to be formed by intermolecular hydrogen bonds in aggregated structures.[42,48,52,53] Relatively tightly wound 3_{10}-helices serve as an intermediary conformation.[42,54] The intensities of β-sheets, α-helices, and antiparallel β-sheets observed in the incubated PrP in sDNA-2.0PrP (D_{30}) were reduced significantly compared to the intensities measured at D_0. This reduction in intensity might result from the interaction between positively charged Lys residues in PrP and DNA phosphates.[55,56]

Figure 6c,d displays the percentages of PrP secondary structures as a function of the PrP concentration and the ratio of percentages of secondary structures in PrP with respect to CoP, respectively. Plots were obtained as percentage values of individual secondary structures for PrP (with and without sDNA) and fold change values were expressed as a percentage of secondary structures in PrP with respect to CoP. Minor components of secondary structures such as 3_{10}-helices, random coils, and β-turns were grouped in others.[48] After incubation, the α-helix fold change drastically increased while the β-sheet fold change decreased, which was consistent with the CD measurement. This suggests an enhanced resistance to

https://doi.org/10.1021/acsomega.1c04328
ACS Omega 2022, 7, 176−186

aggregation of PrP in the presence of DNA molecules in agreement with previous work comparing DNA effects on full-length and PrP peptides showing that while nucleic acids stimulate rPrP23-231 aggregation, they rather prevent the aggregation of hydrophobic domains of PrP[8]. The antiparallel β-sheet content after incubation analyzed by FTIR was increased by 2.5 fold although it was decreased when measured by CD. This discrepancy might be due to the different sample conditions, i.e., solution phase for CD and dry phase for FTIR.

Cell Viability of CoP- and PrP-Bound sDNA Duplexes. Next, we assessed the cytotoxicity of PrP and CoP peptides in the presence and absence of sDNA. Figure 6e shows the fold changes in viable SH-SY5Y cells treated with PrP. As expected, the viability was lower for cells exposed to the highest PrP concentration tested (100 μM) in comparison with cells treated with CoP. Interestingly, the cell viability improved when the PrP peptides were combined with sDNA (i.e., sDNA-PrP). Thus, DNA duplexes contribute to stabilizing PrP peptide structures. These data suggest that the results of our *in vitro* experiments are important for reducing the pathogenic properties of the prion peptide. Consequently, our findings provide important clues in favor of the pathological relevance of the interaction between prion peptides and DNA molecules.

CONCLUSIONS

We generated PrP bound to synthetic DNA lattices and natural DNA duplexes extracted from salmon (sDNA) and investigated their physical characteristics to understand the interaction between DNA and PrP. Topological characteristics of the DNA lattices combined with the PrP peptides were visualized by AFM to determine the influence of PrP during the formation of DNA lattices. We observed that PrP disrupted the growth of the DX lattices more than CoP. We conducted various optical measurements such as UV−Vis, CD, and FTIR spectroscopies to study the structural stability of the DNA and the secondary structures of PrP and to validate the interaction between DNA and PrP. As a result of the interaction of PrP with sDNA, UV−Vis absorbance spectra showed a shift of the absorbance intensities, which were characteristics of CoP and PrP binding to DNA. The CD analysis revealed the presence of various secondary structures, such as α-helices, β-sheets, and antiparallel β-sheets in PrP- and PrP-bound sDNA complexes. FTIR confirmed the PrP−sDNA interaction and the alteration of PrP secondary structures in the presence of DNA. To verify the effect of the PrP-bound sDNA complexes, cytotoxicity assay on human neuroblastoma cells in culture was performed, which reflected the attenuation of the cytotoxicity of PrP with sDNA than CoP. Our work suggests valuable information to exploit this effect in the development of potential therapeutic and medical applications such as novel therapeutic modalities in treating prion toxicity and effective biochemical sensors. In addition, our results provide immense possibilities for all of the various amyloid proteins and their disease pathology.

MATERIALS AND EXPERIMENTAL METHODS

Preparation of the Control (CoP) and Prion Peptides (PrP). Lyophilized synthetic peptides were purchased from BACHEM (Bubendorf, Switzerland). These include PrP—a synthetic prion protein model peptide resembling a portion of the human prion protein in structure and function spanning amino acid residues 106−126 (KTNMKHMAGAAAAGAVVGGLG),[57] and CoP—a control peptide consisting of the same amino acids as PrP106−126 in a scrambled sequence (LVGAHAGKMGANTAKAGAMVG).[57]

Lyophilized peptides were dissolved in 100% 1,1,1,3,3,3-hexafluoro-2-propanol (HFIP), sonicated in a water bath for 2−3 min, and aliquoted into sterile Eppendorf tubes. The HFIP solvent was evaporated in a vacuum desiccator and the peptides were stored at −20 °C.[58] Prior to use, PrP was dissolved in 200 mM acetate buffer (150 mM NaCl, pH 5.5) containing 50% (v/v) acetonitrile at the desired concentration (Figures 1 and Figures 3−6).

Synthesis of DX Lattices Bound with Various Concentrations of PrP ([PrP]). A two-step annealing method to fabricate PrP-bound DX lattices on mica was followed.

In the first step, individual DX tiles[33] (DX1 and DX2) were generated by combining equimolar concentrations of their strands into two separate test tubes. Each DX tile was formed by mixing a stoichiometric quantity of each strand in 1× TAE/Mg^{2+} buffer (40 mM Tris, 20 mM acetic acid, 1 mM EDTA [pH 8.0], and 12.5 mM magnesium acetate). To facilitate the hybridization, they were cooled slowly from 95 to 25 °C by placing the tubes in 2 L of boiled water in a styrofoam box for 48 h. A DX tile concentration of 100 nM was obtained.

In the second step, PrP-bound DX lattices on mica were constructed using the mica-assisted growth (MAG) method. Annealed individual DX tiles (20 nM) with the desired [PrP] were added into a new test tube containing mica (size of 5 mm × 5 mm). To facilitate the hybridization of DX-CoP and DX-PrP lattices on mica, the sample test tubes were kept in a styrofoam box containing 2 L of water at 40 °C, followed by a gradual cooling from 40 to 25 °C. After annealing, the samples were incubated overnight at 4 °C to promote structure stabilization (Figures 1 and 2).

AFM Imaging. AFM imaging was performed by taking the mica substrate out from the test tube and fixing it on a metal puck with instant glue. We added 30 μL of 1× TAE/Mg^{2+} buffer onto the substrate and 20 μL of 1× TAE/Mg^{2+} onto a silicon nitride AFM tip (Veeco Inc., CA). A multimode nanoscope (Veeco Inc., CA) in fluid-tapping mode was used to acquire AFM images (Figure 2).

Preparation of sDNA Solution and Thin Film Binding with PrP. To prepare the homogeneous sDNA solution, 0.1 g of sDNA (DNA enzymatically extracted from salmon, GEM Corporation, Shiga, Japan) was dissolved in 10 mL of deionized water and placed on a magnetic stirrer at 800 rpm overnight at room temperature to obtain 1.0 wt %. For the construction of PrP-bound sDNA duplexes, the sDNA solution (0.1 wt %) was mixed with the desired [PrP] and used for UV−Vis absorbance, CD, and cell viability. For FTIR, 20 μL of the sample of the PrP-bound sDNA solution obtained after incubation for 0 (D_0) or 30 days (D_{30}) was drop-cast on the oxygen plasma-treated glass and dried for 24 h (Figures 1 and Figures 3−6).

Circular Dichroism (CD) and UV−Vis Absorbance. The secondary structures of the pristine PrP- and PrP-bound to sDNA duplexes were assessed by measuring the CD spectrum at 25 °C using a Jasco J-810 CD spectrometer (JASCO, OK). Wavelength scanning was performed for an average of 15 scans at 25 °C with 1.0 mm quartz cells. The spectra were acquired between 190 and 320 nm at 1 nm interval, averaged over 2 s, and at a scanning speed of 200 nm/s. The UV−Vis absorbance was also recorded (Figure 4).

https://doi.org/10.1021/acsomega.1c04328
ACS Omega 2022, 7, 176−186

Fourier Transform Infrared Spectroscopy (FTIR). The FTIR spectra were recorded in the wavenumber range from 4000 to 600 cm^{-1} for thin films of PrP, sDNA, and PrP−sDNA on glass with a TENSOR 27 spectrometer (Detector: MIR_ATR [ZnSe], Bruker Inc., MA). A total of 32 scans were co-added and averaged with a resolution of 4 cm^{-1}. The data in the FTIR spectra are presented after subtraction of the background spectrum produced by glass only (Figure 5).

The curve-fitted FTIR spectra were obtained by using OMNIC software (v7.3, Thermo Scientific, MA). The original amide I spectra were subjected to a second derivative analysis and the resulting spectra were smoothed using a denoising algorithm, the nine-point Savitzky−Golay smoothing filter of polynomial degree 5. Using an enhancement factor of 2 and a bandwidth of 25 cm^{-1}, FSD was performed with a Gaussian line shape generating a spectrum consisting of the same number of components and peak positions as the second derivative spectrum. Gaussian curve fit was obtained using FSD spectra within a ±1 cm^{-1} range through the built-in Levenberg−Marquardt algorithm.[59,60] All of the other parameters were left free to adjust iteratively. Consequently, each secondary structural component in the amide I band was computed as a fractional area of the corresponding peak divided by the sum of the areas of the amide I band peaks[42,48] (Figures 5 and 6).

Cell Culture and Cytotoxicity Assay. The adherent human neuroblastoma SH-SY5Y cell line was cultured in DMEM medium supplemented with 10% fetal calf serum and 1% penicillin/streptomycin (Life Technologies, Inc., CA). Cells in the serum-free DMEM medium were maintained at 37 °C under a humidified 5% CO_2 atmosphere. When being passaged or harvested for analysis, the cells were dissociated using trypsin/EDTA.

A cytotoxicity assay was performed using the EZ Cytox cell viability assay (water-soluble tetrazolium [WST] salt method). The WST reagent solution (10 μL) was added to each well of a 96-well microplate containing 100 μL of cells per well. The plate was then incubated for 3 h at 37 °C. The absorbance was measured at 450 nm using a microplate reader with an appropriate blank to record the background signal. As a result, the cell viability was calculated and expressed as a fold change value against the cells treated with CoP (Figure 6).

AUTHOR INFORMATION

Corresponding Authors

Kyeong Kyu Kim − *Sungkyunkwan Advanced Institute of Nanotechnology (SAINT) and Department of Precision Medicine, School of Medicine, Sungkyunkwan University, Suwon 16419, Korea;* orcid.org/0000-0003-2515-8894; Email: kyeongkyu@skku.edu

Sung Ha Park − *Department of Physics, Sungkyunkwan University, Suwon 16419, Korea; Sungkyunkwan Advanced Institute of Nanotechnology (SAINT), Sungkyunkwan University, Suwon 16419, Korea;* orcid.org/0000-0002-0256-3363; Email: sunghapark@skku.edu

Authors

Anshula Tandon − *Department of Physics, Sungkyunkwan University, Suwon 16419, Korea; Sungkyunkwan Advanced Institute of Nanotechnology (SAINT), Sungkyunkwan University, Suwon 16419, Korea*

Vinod Kumar Subramani − *Department of Precision Medicine, School of Medicine, Sungkyunkwan University, Suwon 16419, Korea*

Complete contact information is available at: https://pubs.acs.org/10.1021/acsomega.1c04328

Author Contributions

‖A.T. and V.K.S. contributed equally to this work. A.T. and V.K.S. initiated the project, designed and performed experiments, analyzed data, and wrote the paper. K.K.K. and S.H.P. initiated and directed the project, designed experiments, analyzed data, and wrote the paper. All authors have given approval to the final version of the manuscript.

Funding

This work was supported by the National Research Foundation (NRF) of Korea (2018R1D1A1B07051065, 2019R1I1A1A01060208, and 2021R1A2C1005279).

Notes

The authors declare no competing financial interest.

ABBREVIATIONS

DNA, deoxyribonucleic acid; sDNA, salmon deoxyribonucleic acid; PrP, prion protein; AFM, atomic force microscopy; DX, double-crossover; UV−Vis, ultraviolet−visible; CD, circular dichroism; FTIR, Fourier transform infrared; MAG, mica-assisted growth; FSD, Fourier self-deconvolution; TAE, Tris-acetate-EDTA; EDTA, ethylene-diamine-tetraacetic acid; FFT, fast Fourier transform

REFERENCES

(1) Prusiner, S. B. Prions. *Proc. Natl. Acad. Sci. U.S.A.* **1998**, *95*, 13363−13383.

(2) Pan, K. M.; Baldwin, M.; Nguyen, J.; Gasset, M.; Serban, A.; Groth, D.; Mehlhorn, I.; Huang, Z.; Fletterick, R. J.; Cohen, F. E. Conversion of Alpha-Helices into Beta-Sheets Features in the Formation of the Scrapie Prion Proteins. *Proc. Natl. Acad. Sci. U.S.A.* **1993**, *90*, 10962−10966.

(3) De Gioia, L.; Selvaggini, C.; Ghibaudi, E.; Diomede, L.; Bugiani, O.; Forloni, G.; Tagliavini, F.; Salmona, M. Conformational Polymorphism of the Amyloidogenic and Neurotoxic Peptide Homologous to Residues 106-126 of the Prion Protein. *J. Biol. Chem.* **1994**, *269*, 7859−7862.

(4) Selvaggini, C.; De Gioia, L.; Cantù, L.; Ghibaudi, E.; Diomede, L.; Passerini, F.; Forloni, G.; Bugiani, O.; Tagliavini, F.; Salmona, M. Molecular Characteristics of a Protease-Resistant, Amyloidogenic and Neurotoxic Peptide Homologous to Residues 106-126 of the Prion Protein. *Biochem. Biophys. Res. Commun.* **1993**, *194*, 1380−1386.

(5) Forloni, G.; Angeretti, N.; Malesani, P.; Peressini, E.; Rodriguez Martin, T.; Della Torre, P.; Salmona, M. Influence of Mutations Associated with Familial Prion-Related Encephalopathies on Biological Activity of Prion Protein Peptides. *Ann. Neurol.* **1999**, *45*, 489−494.

(6) Caughey, B.; Raymond, G. J. Sulfated Polyanion Inhibition of Scrapie-Associated PrP Accumulation in Cultured Cells. *J. Virol.* **1993**, *67*, 643−650.

(7) DebBurman, S. K.; Raymond, G. J.; Caughey, B.; Lindquist, S. Chaperone-Supervised Conversion of Prion Protein to Its Protease-Resistant Form. *Proc. Natl. Acad. Sci. U.S.A.* **1997**, *94*, 13938−13943.

(8) Cordeiro, Y.; Machado, F.; Juliano, L.; Juliano, M. A.; Brentani, R. R.; Foguel, D.; Silva, J. L. DNA Converts Cellular Prion Protein into the Beta-Sheet Conformation and Inhibits Prion Peptide Aggregation. *J. Biol. Chem.* **2001**, *276*, 49400−49409.

(9) Wong, C.; Xiong, L. W.; Horiuchi, M.; Raymond, L.; Wehrly, K.; Chesebro, B.; Caughey, B. Sulfated Glycans and Elevated Temper-

https://doi.org/10.1021/acsomega.1c04328
ACS Omega 2022, 7, 176−186

ature Stimulate PrP(Sc)-Dependent Cell-Free Formation of Protease-Resistant Prion Protein. *EMBO J.* **2001**, *20*, 377−386.
(10) Deleault, N. R.; Geoghegan, J. C.; Nishina, K.; Kascsak, R.; Williamson, R. A.; Supattapone, S. Protease-Resistant Prion Protein Amplification Reconstituted with Partially Purified Substrates and Synthetic Polyanions. *J. Biol. Chem.* **2005**, *280*, 26873−26879.
(11) Silva, J. L.; Gomes, M. P. B.; Vieira, T. C. R. G.; Cordeiro, Y. PrP Interactions with Nucleic Acids and Glycosaminoglycans in Function and Disease. *Front. Biosci.* **2010**, *15*, 132−150.
(12) Silva, J. L.; Lima, L. M. T. R.; Foguel, D.; Cordeiro, Y. Intriguing Nucleic-Acid-Binding Features of Mammalian Prion Protein. *Trends Biochem. Sci.* **2008**, *33*, 132−140.
(13) Weissmann, C. A. "unified Theory" of Prion Propagation. *Nature* **1991**, *352*, 679−683.
(14) Watt, N. T.; Routledge, M. N.; Wild, C. P.; Hooper, N. M. Cellular Prion Protein Protects against Reactive-Oxygen-Species-Induced DNA Damage. *Free Radical Biol. Med.* **2007**, *43*, 959−967.
(15) Bravard, A.; Auvré, F.; Fantini, D.; Bernardino-Sgherri, J.; Sissoëff, L.; Daynac, M.; Xu, Z.; Etienne, O.; Dehen, C.; Comoy, E.; et al. The Prion Protein Is Critical for DNA Repair and Cell Survival after Genotoxic Stress. *Nucleic Acids Res.* **2015**, *43*, 904−916.
(16) Takemura, K.; Wang, P.; Vorberg, I.; Surewicz, W.; Priola, S. A.; Kanthasamy, A.; Pottathil, R.; Chen, S. G.; Sreevatsan, S. DNA Aptamers That Bind to PrPC and Not PrpSc Show Sequence and Structure Specificity. *Exp. Biol. Med.* **2006**, *231*, 204−214.
(17) Matsugami, A.; Ouhashi, K.; Kanagawa, M.; Liu, H.; Kanagawa, S.; Uesugi, S.; Katahira, M. An Intramolecular Quadruplex of (GGA) (4) Triplet Repeat DNA with a G:G:G:G Tetrad and a G(:A):G-(:A):G(:A):G Heptad, and Its Dimeric Interaction. *J. Mol. Biol.* **2001**, *313*, 255−269.
(18) Nandi, P. K.; Nicole, J.-C. Nucleic Acid and Prion Protein Interaction Produces Spherical Amyloids Which Can Function in Vivo as Coats of Spongiform Encephalopathy Agent. *J. Mol. Biol.* **2004**, *344*, 827−837.
(19) Nandi, P. K.; Leclerc, E. Polymerization of Murine Recombinant Prion Protein in Nucleic Acid Solution. *Arch. Virol.* **1999**, *144*, 1751−1763.
(20) Takemura, K.; Wang, P.; Vorberg, I.; Surewicz, W.; Priola, S. A.; Kanthasamy, A.; Pottathil, R.; Chen, S. G.; Sreevatsan, S. DNA Aptamers That Bind to PrP^{C} and Not Prp^{Sc} Show Sequence and Structure Specificity. *Exp. Biol. Med.* **2006**, *231*, 204−214.
(21) Macedo, B.; Millen, T. A.; Braga, C. A. C. A.; Gomes, M. P. B.; Ferreira, P. S.; Kraineva, J.; Winter, R.; Silva, J. L.; Cordeiro, Y. Nonspecific Prion Protein−Nucleic Acid Interactions Lead to Different Aggregates and Cytotoxic Species. *Biochemistry* **2012**, *51*, 5402−5413.
(22) Karpuj, M. V.; Gelibter-Niv, S.; Tiran, A.; Rambold, A.; Tatzelt, J.; Nunziante, M.; Schatzl, H. M. Conditional Modulation of Membrane Protein Expression in Cultured Cells Mediated by Prion Protein Recognition of Short Phosphorothioate Oligodeoxynucleotides. *J. Biol. Chem.* **2011**, *286*, 6911−6917.
(23) Kocisko, D. A.; Vaillant, A.; Lee, K. S.; Arnold, K. M.; Bertholet, N.; Race, R. E.; Olsen, E. A.; Juteau, J.-M.; Caughey, B. Potent Antiscrapie Activities of Degenerate Phosphorothioate Oligonucleotides. *Antimicrob. Agents Chemother.* **2006**, *50*, 1034−1044.
(24) Wang, L.; Yoshida, J.; Ogata, N.; Sasaki, S.; Kajiyama, T. Self-Assembled Supramolecular Films Derived from Marine Deoxyribonucleic Acid (DNA)−Cationic Surfactant Complexes: Large-Scale Preparation and Optical and Thermal Properties. *Chem. Mater.* **2001**, *13*, 1273−1281.
(25) Zhang, G.; Wang, L.; Yoshida, J.; Ogata, N. Optical and Optoelectronic Materials Derived from Biopolymer Deoxyribonucleic Acid (DNA). *SPIE Proc.* **2001**, *4580*, No. 444982.
(26) Forloni, G.; Angeretti, N.; Chiesa, R.; Monzani, E.; Salmona, M.; Bugiani, O.; Tagliavini, F. Neurotoxicity of a Prion Protein Fragment. *Nature* **1993**, *362*, 543−546.
(27) O'Donovan, C. N.; Tobin, D.; Cotter, T. G. Prion Protein Fragment PrP-(106−126) Induces Apoptosis via Mitochondrial Disruption in Human Neuronal SH-SY5Y Cells. *J. Biol. Chem.* **2001**, *276*, 43516−43523.
(28) Brown, D. R.; Schmidt, B.; Kretzschmar, H. A. Role of Microglia and Host Prion Protein in Neurotoxicity of a Prion Protein Fragment. *Nature* **1996**, *380*, 345−347.
(29) Florio, T.; Thellung, S.; Amico, C.; Robello, M.; Salmona, M.; Bugiani, O.; Tagliavini, F.; Forloni, G.; Schettini, G. Prion Protein Fragment 106-126 Induces Apoptotic Cell Death and Impairment of L-Type Voltage-Sensitive Calcium Channel Activity in the GH3 Cell Line. *J. Neurosci. Res.* **1998**, *54*, 341−352.
(30) Tagliavini, F.; Prelli, F.; Verga, L.; Giaccone, G.; Sarma, R.; Gorevic, P.; Ghetti, B.; Passerini, F.; Ghibaudi, E.; Forloni, G. Synthetic Peptides Homologous to Prion Protein Residues 106-147 Form Amyloid-like Fibrils in Vitro. *Proc. Natl. Acad. Sci. U.S.A.* **1993**, *90*, 9678−9682.
(31) Fioriti, L.; Quaglio, E.; Massignan, T.; Colombo, L.; Stewart, R. S.; Salmona, M.; Harris, D. A.; Forloni, G.; Chiesa, R. The Neurotoxicity of Prion Protein (PrP) Peptide 106-126 Is Independent of the Expression Level of PrP and Is Not Mediated by Abnormal PrP Species. *Mol. Cell. Neurosci.* **2005**, *28*, 165−176.
(32) Nandi, P. K. Interaction of Prion Peptide HuPrP106−126 with Nucleic Acid. *Arch. Virol.* **1997**, *142*, 2537−2545.
(33) Winfree, E.; Liu, F.; Wenzler, L. A.; Seeman, N. C. Design and Self-Assembly of Two-Dimensional DNA Crystals. *Nature* **1998**, *394*, 539−544.
(34) Blackley, H. K.; Sanders, G. H.; Davies, M. C.; Roberts, C. J.; Tendler, S. J.; Wilkinson, M. J. In-Situ Atomic Force Microscopy Study of Beta-Amyloid Fibrillization. *J. Mol. Biol.* **2000**, *298*, 833−840.
(35) Lee, J.; Hamada, S.; Hwang, S. U.; Amin, R.; Son, J.; Dugasani, S. R.; Murata, S.; Park, S. H. Quantitative Analysis of Molecular-Level DNA Crystal Growth on a 2D Surface. *Sci. Rep.* **2013**, *3*, No. 2115.
(36) Miyahara, T.; Nakatsuji, H.; Sugiyama, H. Helical Structure and Circular Dichroism Spectra of DNA: A Theoretical Study. *J. Phys. Chem. A* **2013**, *117*, 42−55.
(37) Li, H. J.; Epstein, P.; Yu, S. S.; Brand, B. Investigation of Huge Negative Circular Dichroism Spectra of Some Nucleoproteins. *Nucleic Acids Res.* **1974**, *1*, 1371−1383.
(38) Johnson, B. B.; Dahl, K. S.; Tinoco, I.; Ivanov, V. I.; Zhurkin, V. B. Correlations between Deoxyribonucleic Acid Structural Parameters and Calculated Circular Dichroism Spectra. *Biochemistry* **1981**, *20*, 73−78.
(39) Micsonai, A.; Wien, F.; Bulyáki, É.; Kun, J.; Moussong, É.; Lee, Y.-H.; Goto, Y.; Réfrégiers, M.; Kardos, J. BeStSel: A Web Server for Accurate Protein Secondary Structure Prediction and Fold Recognition from the Circular Dichroism Spectra. *Nucleic Acids Res.* **2018**, *46*, W315−W322.
(40) Church, G. M.; Sussman, J. L.; Kim, S. H. Secondary Structural Complementarity between DNA and Proteins. *Proc. Natl. Acad. Sci. U.S.A.* **1977**, *74*, 1458−1462.
(41) Krimm, S.; Bandekar, J. Vibrational Spectroscopy and Conformation of Peptides, Polypeptides, and Proteins. In *Advances in Protein Chemistry*; Elsevier, 1986; Vol. *38*, pp 181−364.
(42) Jackson, M.; Mantsch, H. H. The Use and Misuse of FTIR Spectroscopy in the Determination of Protein Structure. *Crit. Rev. Biochem. Mol. Biol.* **1995**, *30*, 95−120.
(43) Tajmir-Riahi, H. A.; N'soukpoé-Kossi, C. N.; Joly, D. Structural Analysis of Protein−DNA and Protein−RNA Interactions by FTIR, UV-Visible and CD Spectroscopic Methods. *Spectroscopy* **2009**, *23*, 81−101.
(44) Wood, B. R. The Importance of Hydration and DNA Conformation in Interpreting Infrared Spectra of Cells and Tissues. *Chem. Soc. Rev.* **2016**, *45*, 1980−1998.
(45) Barth, A. Infrared Spectroscopy of Proteins. *Biochim. Biophys. Acta* **2007**, *1767*, 1073−1101.
(46) Kauppinen, J. K.; Moffatt, D. J.; Mantsch, H. H.; Cameron, D. G. Fourier Self-Deconvolution: A Method for Resolving Intrinsically Overlapped Bands. *Appl. Spectrosc.* **1981**, *35*, 271−276.

https://doi.org/10.1021/acsomega.1c04328
ACS Omega 2022, 7, 176−186

(47) Rahmelow, K.; Hübner, W. Fourier Self-Deconvolution: Parameter Determination and Analytical Band Shapes. *Appl. Spectrosc.* **1996**, *50*, 795−804.
(48) Byler, D. M.; Susi, H. Examination of the Secondary Structure of Proteins by Deconvolved FTIR Spectra. *Biopolymers* **1986**, *25*, 469−487.
(49) Arrondo, J. L. R.; Muga, A.; Castresana, J.; Goñi, F. M. Quantitative Studies of the Structure of Proteins in Solution by Fourier-Transform Infrared Spectroscopy. *Prog. Biophys. Mol. Biol.* **1993**, *59*, 23−56.
(50) Susi, H.; Byler, D. M. Resolution-Enhanced Fourier Transform Infrared Spectroscopy of Enzymes. *Methods Enzymol.* **1986**, *130*, 290−311.
(51) Satheeshkumar, K. S.; Jayakumar, R. Conformational Polymorphism of the Amyloidogenic Peptide Homologous to Residues 113−127 of the Prion Protein. *Biophys. J.* **2003**, *85*, 473−483.
(52) Clark, A. H.; Saunderson, D. H. P.; Suggett, A. Infrared and Laser-Raman Spectroscopic Studies of Thermally-Induced Protein Gels. *Int. J. Pept. Protein Res.* **1981**, *17*, 353−364.
(53) Jung, C. Insight into Protein Structure and Protein-Ligand Recognition by Fourier Transform Infrared Spectroscopy. *J. Mol. Recognit.* **2000**, *13*, 325−351.
(54) Kennedy, D. F.; Crisma, M.; Toniolo, C.; Chapman, D. Studies of Peptides Forming 310- and.Alpha.-Helixes and.Beta.-Bend Ribbon Structures in Organic Solution and in Model Biomembranes by Fourier Transform Infrared Spectroscopy. *Biochemistry* **1991**, *30*, 6541−6548.
(55) Uma Maheswari, P.; Palaniandavar, M. DNA Binding and Cleavage Properties of Certain Tetrammine Ruthenium(II) Complexes of Modified 1,10-Phenanthrolines − Effect of Hydrogen-Bonding on DNA-Binding Affinity. *J. Inorg. Biochem.* **2004**, *98*, 219−230.
(56) Nandi, P. K. Interaction of Prion Peptide HuPrP106−126 with Nucleic Acid. *Arch. Virol.* **1997**, *142*, 2537−2545.
(57) Grabenauer, M.; Wu, C.; Soto, P.; Shea, J.-E.; Bowers, M. T. Oligomers of the Prion Protein Fragment 106−126 Are Likely Assembled from β-Hairpins in Solution, and Methionine Oxidation Inhibits Assembly without Altering the Peptide's Monomeric Conformation. *J. Am. Chem. Soc.* **2010**, *132*, 532−539.
(58) Kanapathipillai, M.; Ku, S. H.; Girigoswami, K.; Park, C. B. Small Stress Molecules Inhibit Aggregation and Neurotoxicity of Prion Peptide 106−126. *Biochem. Biophys. Res. Commun.* **2008**, *365*, 808−813.
(59) Goormaghtigh, E.; Cabiaux, V.; Ruysschaert, J.-M. Determination of Soluble and Membrane Protein Structure by Fourier Transform Infrared Spectroscopy. In *Physicochemical Methods in the Study of Biomembranes*; Hilderson, H. J.; Ralston, G. B., Eds.; Springer: US, 1994; Vol. *23*, pp 405−450.
(60) Lórenz-Fonfría, V. A.; Padrós, E. Curve-Fitting of Fourier Manipulated Spectra Comprising Apodization, Smoothing, Derivation and Deconvolution. *Spectrochim. Acta, Part A* **2004**, *60*, 2703−2710.

https://doi.org/10.1021/acsomega.1c04328
ACS Omega 2022, 7, 176−186